

Article

Frequency Power Spectra of Global Quantities in Unsteady Magnetoconvection

Sandip Das and Krishna Kumar *

Department of Physics, Indian Institute of Technology Kharagpur, Kharagpur 721302, India; d.sandip@phy.iitkgp.ernet.in

* Correspondence: kumar.phy.iitkgp@gmail.com

Abstract: We present the results of direct numerical simulations of power spectral densities for kinetic energy, convective entropy, and heat flux for unsteady Rayleigh–Bénard magnetoconvection in the frequency space. For larger values of frequency, the power spectral densities for all the global quantities vary with frequency (f) as f^{-2} . The scaling exponent is independent of Rayleigh number, Chandrasekhar’s number, and thermal Prandtl number.

Keywords: magnetoconvection; turbulent flow; power spectral densities (PSD)

1. Introduction

The temporal fluctuations [1] of spatially averaged (or, global) quantities are of interest in several fields of research, including turbulent flows [2–7], nanofluids [8], biological fluids [9,10], geophysics [11,12], and phase transitions [13,14]. The probability density function (PDF) of the temporal fluctuations of thermal flux in turbulent Rayleigh–Bénard convection (RBC) was found to have normal distribution with slight asymmetries near the tails. Aumaitre and Fauve [5] also showed that the statistical properties of locally measured and globally averaged temperature field are quite different. They found that the power spectra of Nusselt number (Nu), which is a measure of heat flux across the fluid layer in RBC, varies with frequency (f) as f^{-2} at higher frequencies. The scaling exponent for the temperature field that is measured near the lower and upper boundaries is different from the one that is measured in the central part of the experimental cell. The direct numerical simulations (DNS) of the Nusselt number (Nu) also showed the similar behaviour in the presence of Lorentz force [15] in water-based nanofluids ($Pr = 4.0$). The power spectral density (PSD) of the thermal flux in the frequency (f) space [2,5,15,16] was found to vary as f^{-2} . The frequency spectrum for the temperature field measured near the horizontal plates in Rayleigh–Bénard magnetoconvection [17] shows the exponent to vary between -6 and -4 . The frequency spectra of kinetic energy and convective entropy for the problem of magnetoconvection are rarely available, either experimentally or numerically. The frequency spectrum for the Nusselt number [15] was recently computed only for one value of the thermal Prandtl number.

In this work, we present the results that were obtained by DNS for the frequency spectra of three global quantities: spatially averaged kinetic energy per unit mass (E), convective entropy per unit mass (E_{\ominus}), and Nusselt number (Nu) in unsteady Rayleigh–Bénard magnetoconvection (RBM) [18–20] for several values of Rayleigh number (Ra), Prandtl number (Pr), and Chandrasekhar number (Q). The objective is to study the statistical properties of the fluctuating global quantities in Rayleigh–Bénard magnetoconvection. The kinetic energy per unit mass as well as the convective entropy per unit mass are found to vary with frequency as f^{-2} at relatively higher frequencies. This behaviour does not depend on the Rayleigh number (Ra), Prandtl number (Pr), and Chandrasekhar’s number (Q).



Citation: Das, S.; Kumar, K. Frequency Power Spectra of Global Quantities in Unsteady Magnetoconvection. *Fluids* **2021**, *6*, 163. <https://doi.org/10.3390/fluids6040163>

Academic Editor: Ioannis Sarris

Received: 5 March 2021

Accepted: 8 April 2021

Published: 19 April 2021

Publisher’s Note: MDPI stays neutral with regard to jurisdictional claims in published maps and institutional affiliations.



Copyright: © 2021 by the authors. Licensee MDPI, Basel, Switzerland. This article is an open access article distributed under the terms and conditions of the Creative Commons Attribution (CC BY) license (<https://creativecommons.org/licenses/by/4.0/>).

2. Governing Equations

The physical system consists of a thin layer of a Boussinesq fluid (e.g., liquid metals, melts of some alloys (i.e., $NaNO_3$ melt), nanofluids, etc.) of density ρ_0 and electrical conductivity σ confined between two horizontal plates, which are made of electrically non-conducting, but thermally conducting materials. The lower plate is heated uniformly and the upper plate is cooled uniformly, so that an adverse temperature gradient β is maintained across the fluid layer. A uniform magnetic field B_0 is applied in the vertical upward direction, which is also considered the positive direction of the z -axis. The x and y axes are in the horizontal plane with origin of the coordinate system taken on the lower plate. In the basic state, the fluid conducts heat without any motion. The stratification of the steady temperature field $[T_s(z)]$ and the fluid density $[\rho_s(z)]$, in the conduction state [18], are given as:

$$T_s(z) = T_b - \beta z, \tag{1}$$

$$\rho_s(z) = \rho_0[1 + \alpha\{T_b - T_s(z)\}], \tag{2}$$

where T_b and ρ_0 are the temperature and density of the fluid at the lower plate, respectively. The fluid pressure $[P_s(z)]$, in conductive state, is:

$$P_s(z) = C - \left[\rho_0 g \left(z + \frac{1}{2} \alpha \beta z^2 \right) + \frac{B_0^2}{2\mu_0} \right], \tag{3}$$

where g is the acceleration due to gravity and μ_0 is the permeability of free space. The fluid pressure in the conductive state consists of hydrostatic, thermal, and magnetic pressures. The constant of integration (C) may be determined if the value of pressure at the upper plate $[P_s(z = d)]$ is known. If we take $P_s(z = d) = P_0$, where P_0 is a constant (e.g., air pressure at the upper plate), the constant C turns out to be

$$C = P_0 + \frac{B_0^2}{2\mu_0} + \left[\rho_0 g \left(d + \frac{1}{2} \alpha \beta d^2 \right) \right]. \tag{4}$$

The fluid pressure, in the basic conductive state, then reads as:

$$P_s(z) = P_0 + \rho_0 g \left[(d - z) + \frac{1}{2} \alpha \beta (d^2 - z^2) \right]. \tag{5}$$

As soon as the temperature gradient across the fluid layer is raised above a critical value β_c for fixed values of all fluid parameters (kinematic viscosity ν , thermal diffusivity κ , and thermal expansion coefficient α) and the externally imposed magnetic field (B_0), the convection sets in. All the fields are perturbed due to magnetoconvection and they may be expressed as:

$$\rho_s(z) \rightarrow \tilde{\rho}(x, y, z, t) = \rho_s(z) + \delta\rho(x, y, z, t), \tag{6}$$

$$T_s(z) \rightarrow T(x, y, z, t) = T_s(z) + \theta(x, y, z, t), \tag{7}$$

$$P_s(z) \rightarrow P(x, y, z, t) = P_s(z) + p(x, y, z, t), \tag{8}$$

$$\mathbf{B}_0 \rightarrow \mathbf{B}(x, y, z, t) = \mathbf{B}_0 + \mathbf{b}(x, y, z, t), \tag{9}$$

where $\mathbf{v}(x, y, z, t)$, $p(x, y, z, t)$, $\theta(x, y, z, t)$ and $\mathbf{b}(x, y, z, t)$ are the fluid velocity, perturbation in the fluid pressure, the convective temperature and the induced magnetic field, respectively, due to magnetoconvection. The perturbative fields are made dimensionless by measuring all lengths in units of the clearance d between two horizontal plates, which is also the thickness of the fluid layer. Time is measured in units of the free fall time $\tau_f = 1/\sqrt{\alpha\beta g}$. The convective temperature field θ and induced magnetic field \mathbf{b} are made

dimensionless by βd and $B_0 \text{Pm}$, respectively. The magnetoconvective dynamics is then described by the following dimensionless equations:

$$D_t \mathbf{v} = -\nabla p + \sqrt{\frac{\text{Pr}}{\text{Ra}}} \nabla^2 \mathbf{v} + \frac{\text{QPr}}{\text{Ra}} [\partial_z \mathbf{b} + \text{Pm}(\mathbf{b} \cdot \nabla) \mathbf{b}] + \theta \mathbf{e}_3, \tag{10}$$

$$\text{Pm} D_t \mathbf{b} = \text{Pm}(\mathbf{b} \cdot \nabla) \mathbf{v} + \sqrt{\frac{\text{Pr}}{\text{Ra}}} \nabla^2 \mathbf{b} + \partial_z \mathbf{v}, \tag{11}$$

$$D_t \theta = \sqrt{\frac{1}{\text{RaPr}}} \nabla^2 \theta + v_3, \tag{12}$$

$$\nabla \cdot \mathbf{v} = \nabla \cdot \mathbf{b} = 0, \tag{13}$$

where $D_t \equiv \partial_t + (\mathbf{v} \cdot \nabla)$ is the material derivative. The unit vector \mathbf{e}_3 is directed vertically upward. Because the magnetic Prandtl number is very small ($\text{Pm} \leq 10^{-5}$) for all terrestrial fluids, we set Pm equal to zero in the above set of hydrodynamic equations. The Navier–Stokes equation Equation (10) then takes the form, as given below.

$$D_t \mathbf{v} = -\nabla p + \sqrt{\frac{\text{Pr}}{\text{Ra}}} \nabla^2 \mathbf{v} + \frac{\text{QPr}}{\text{Ra}} \partial_z \mathbf{b} + \theta \mathbf{e}_3. \tag{14}$$

The induced magnetic field (\mathbf{b}) is slaved to the velocity field (\mathbf{v}), as Equation (11) is simplified to

$$\nabla^2 \mathbf{b} = -\sqrt{\frac{\text{Ra}}{\text{Pr}}} \partial_z \mathbf{v}. \tag{15}$$

The fluid flow due to magnetoconvection, in the limit of $\text{Pm} \rightarrow 0$, is described by the set of Equations (12)–(15). We consider the idealized boundary (*stress-free*) conditions for the velocity field on the horizontal boundaries. Relevant boundary conditions [18,21] at the horizontal plates, which are located at $z = 0$ and $z = 1$, are:

$$\frac{\partial v_1}{\partial z} = \frac{\partial v_2}{\partial z} = v_3 = b_1 = b_2 = \frac{\partial b_3}{\partial z} = \theta = 0. \tag{16}$$

All of the fields are considered periodic in the horizontal plane. The fluid dynamics, as $\text{Pm} \rightarrow 0$, is controlled by three dimensionless parameters: (1) Rayleigh number ($\text{Ra} = \frac{\alpha \beta g d^4}{\nu \kappa}$), (2) Prandtl number ($\text{Pr} = \frac{\nu}{\kappa}$), and (3) Chandrasekhar’s number ($\text{Q} = \frac{\sigma B_0^2 d^2}{\rho_0 \nu}$). The critical values of Rayleigh number [$\text{Ra}_c(\text{Q})$] and critical wave number [$k_c(\text{Q})$] are [18]:

$$\text{Ra}_c(\text{Q}) = \frac{\pi^2 + k_c^2}{k_c^2} [(\pi^2 + k_c^2)^2 + \pi^2 \text{Q}], \tag{17}$$

$$k_c(\text{Q}) = \pi \sqrt{a_+ + a_- - \frac{1}{2}}, \text{ where} \tag{18}$$

$$a_{\pm}(\text{Q}) = \left(\frac{1}{4} \left[\frac{1}{2} + \frac{\text{Q}}{\pi^2} \pm \left\{ \left(\frac{1}{2} + \frac{\text{Q}}{\pi^2} \right)^2 - \frac{1}{4} \right\}^{\frac{1}{2}} \right] \right)^{\frac{1}{3}}. \tag{19}$$

The kinetic energy (E) and convective entropy (E_{Θ}) per unit mass are defined as:

$$E(t) = \frac{1}{V} \int_0^{\frac{2\pi}{k_c}} dx \int_0^{\frac{2\pi}{k_c}} dy \int_0^1 \frac{1}{2} v^2 dz, \tag{20}$$

$$E_{\Theta}(t) = \frac{1}{V} \int_0^{\frac{2\pi}{k_c}} dx \int_0^{\frac{2\pi}{k_c}} dy \int_0^1 \frac{1}{2} \theta^2 dz. \tag{21}$$

The Nusselt number (Nu), which is the ratio of total heat flux and the conductive heat flux across the fluid layer, is given as:

$$\text{Nu}(t) = 1 + \frac{\sqrt{\text{RaPr}}}{V} \int_0^{\frac{2\pi}{k_c}} dx \int_0^{\frac{2\pi}{k_c}} dy \int_0^1 v_3 \theta dV. \tag{22}$$

The hydromagnetic system of Equations (12)–(15) presented here may also be used to investigate magnetoconvection in nanofluids with a low concentration of non-magnetic metallic nanoparticles [15] in water. A homogeneous suspension of nanoparticles in a viscous fluid works as a nanofluid. Because the properties of a nanofluid depend on those of the base fluid and the nanoparticles, the effective values of dimensionless parameters would depend on both. All of the fluid parameters are may be replaced by their effective values in the presence of nanoparticles. If ϕ is the volume fraction of the spherically shaped nanoparticles, then the effective form of the density and electrical conductivity of a nanofluid may be expressed as:

$$\rho_{nf} = (1 - \phi)\rho_f + \phi\rho_p, \tag{23}$$

$$\sigma_{nf} = (1 - \phi)\sigma_f + \phi\sigma_p, \tag{24}$$

where ρ_f and σ_f are the density and electrical conductivity of the base fluid, respectively. Here, ρ_p is the density and σ_p is the electrical conductivity of nanoparticles. The effective thermal conductivity (K_{nf}) of a nanofluid [22] for smaller values of ϕ is expressed as:

$$K_{nf} = K_f \left[\frac{(K_p + 2K_f) - 2\phi(K_f - K_p)}{(K_p + 2K_f) + \phi(K_f - K_p)} \right], \tag{25}$$

where K_f and K_p are the thermal conductivities of the base fluid and that of sphere shaped nanoparticles, respectively. Similarly, the product of density and specific heat capacity [$(\rho c_V)_{nf}$] may be expressed through the following relation [23]:

$$(\rho c_V)_{nf} = (1 - \phi)(\rho c_V)_f + \phi(\rho c_V)_p. \tag{26}$$

The effective dynamic viscosity (μ_{nf}) of a nano-fluid [24] may also be expressed as:

$$\mu_{nf} = \mu_f(1 - \phi)^{-2.5}. \tag{27}$$

The kinematic viscosity (ν_{nf}) and thermal diffusivity (κ_{nf}) for nanofluids may then be estimated while using the formulae:

$$\nu_{nf} = \frac{\mu_{nf}}{\rho_{nf}} = \frac{\mu_f(1 - \phi)^{-2.5}}{(1 - \phi)\rho_f + \phi\rho_p}, \tag{28}$$

$$\kappa_{nf} = \frac{K_{nf}}{(\rho c_V)_{nf}} = \frac{K_f \left[(K_p + 2K_f) - 2\phi(K_f - K_p) \right]}{\left[(1 - \phi)(\rho c_V)_f + \phi(\rho c_V)_p \right] \left[(K_p + 2K_f) + \phi(K_f - K_p) \right]}. \tag{29}$$

The effective thermal Prandtl number (Pr_{nf}) for nanofluids is then defined as $\text{Pr}_{nf} = \frac{\nu_{nf}}{\kappa_{nf}}$. The definitions of Rayleigh number (Ra_{nf}) and Chandrasekhar’s number (Q_{nf}) are also modified for nanofluids, and they read as:

$$\text{Ra}_{nf} = \frac{\alpha \beta g d^4}{\nu_{nf} \kappa_{nf}}, \quad \text{Q}_{nf} = \frac{\sigma_{nf} B_0^2 d^2}{(\rho_0)_{nf} \nu_{nf}}. \tag{30}$$

Substituting the values of dimensionless parameters Pr, Ra and Q by Pr_{nf} , Ra_{nf} and Q_{nf} , respectively, the set of Equations (12)–(15) describes magnetoconvection in nanofluids with low concentration of nanoparticles in a base fluid. The thermal Prandtl number (Pr_{nf})

of water-based nanofluids may be varied between 4.0 and 6.5 by varying the volume fraction (ϕ) of the spherical copper nanoparticles [15] between 8% to 0.2%.

3. Direct Numerical Simulations

Direct numerical simulations of the magnetoconvective flows for different values of the dimensionless parameters are carried out using pseudo-spectral method. All of the perturbative fields are expanded such that they are consistent with the boundary conditions. Perturbations are expanded as:

$$\Psi(x, y, z, t) = \sum_{l,m,n} \Psi_{lmn}(t) e^{ik_c(lx+my)} \cos(n\pi z), \tag{31}$$

$$\Phi(x, y, z, t) = \sum_{l,m,n} \Phi_{lmn}(t) e^{ik_c(lx+my)} \sin(n\pi z), \tag{32}$$

where $\Psi(x, y, z, t) = [v_1, v_2, p]^\dagger$ and $\Phi(x, y, z, t) = [v_3, \theta]^\dagger$. The time dependent Fourier amplitudes of these fields are denoted by $\Psi_{lmn}(t) = [U_{lmn}, V_{lmn}, P_{lmn}]^\dagger$ and $\Phi_{lmn}(t) = [W_{lmn}, \Theta_{lmn}]^\dagger$, where l, m , and n are integers. The horizontal wave vector of all the perturbations is $\mathbf{k}_H = (l\mathbf{e}_1 + m\mathbf{e}_2)k_c(Q)$, where \mathbf{e}_1 and \mathbf{e}_2 are the unit vectors along positive directions of the x - and y -axes, respectively. All of the numerical simulations are carried out in a three dimensional simulation box of size $L \times L \times 1$, where $L = 2\pi/k_c(Q)$. The value of k_c is computed using the expression for the critical wave number $k_c(Q)$ [see Equations (18) and (19)]. The continuity equations decide the possible values of the integers l, m, n . They can take values that satisfy the following equation.

$$ilk_c(Q)U_{lmn} + imk_c(Q)V_{lmn} + n\pi W_{lmn} = 0. \tag{33}$$

The computation of non-linear terms $(\mathbf{v} \cdot \nabla)\mathbf{v}$ and $\mathbf{v} \cdot \nabla\theta$ are computed while using Fast Fourier Transformation (FFT). It is done using the following steps:

- (i) Real space variables $\mathbf{v}(x, y, z) = (v_1, v_2, v_3)$ and $\theta(x, y, z)$ are computed at a given time t using inverse FFT of $\mathbf{v}(\mathbf{k})$ and $\theta(\mathbf{k})$, where $\mathbf{k} = lk_c\mathbf{e}_1 + mk_c\mathbf{e}_2 + n\pi\mathbf{e}_3$.
- (ii) The multiplication of field variables $v_i(x, y, z)v_j(x, y, z)$ and $v_i(x, y, z)\theta(x, y, z)$ for $(i, j = 1, 2, 3)$ are done at each grid point of the simulation box.
- (iii) $\text{FFT}[v_i(x, y, z)v_j(x, y, z)]$ and $\text{FFT}[v_i(x, y, z)\theta(x, y, z)]$ are computed using the package FFTW.
- (iv) Subsequently, the terms $ik_j \times \text{FFT}[v_i(x, y, z)v_j(x, y, z)]$ and $ik_j \times \text{FFT}[v_i(x, y, z)\theta(x, y, z)]$ with $j = 1, 2$ as well as $ik_j \times \text{FFT}[v_i(x, y, z)v_j(x, y, z)]$ and $ik_j \times \text{FFT}[v_i(x, y, z)\theta(x, y, z)]$ with $j = 3$ are computed.

The aliasing error is removed using 2/3-rule [25]. The integration in time is performed using a standard fourth order Runge–Kutta (RK4) scheme. The time step of RK4 integration scheme was monitored, so that the Courant–Friedrichs–Lewy (CFL) condition was satisfied for all times. The time step of 10^{-3} (in dimensionless units) is used for integration. The data points for the temporal signal of all global quantities are recorded at all time steps. The grid size was chosen, such that the smallest dissipative (Kolmogorov) scale is resolved. The thermal dissipative scale was the smallest for our simulations. A resolutions of $128 \times 128 \times 128$ was good enough for several of the simulations that are presented here. Each of the simulations was usually carried out for more than 600 dimensionless time units. For $Pr > 1$, we carried the simulations with higher resolutions of $256 \times 256 \times 256$. Das and Kumar [15] test the code for a magnetoconvection problem, which give more details about the simulations. Once a simulation for fixed values of dimensionless parameters Ra, Pr and Q is completed, the same procedure is repeated with a new set of Ra, Pr , and Q .

4. Results and Discussion

The simulations are done for several values of thermal Prandtl number ($0.1 \leq Pr \leq 6.4$). These values of Pr are relevant for Earth’s liquid outer core [26]. They are also relevant

for the problem of crystal growth [27] and water-based nanofluids [8]. The Rayleigh number is varied in a range $7.0 \times 10^4 \leq Ra \leq 3.04 \times 10^6$, while the Chandrasekhar's number is varied in the range $50 \leq Q \leq 10^3$. In numerical simulations, the value of $\Delta T = T_b - T_u$ is always mapped to unity. The total temperature field $[\tilde{T}(x, y, z, t)]$, in the dimensionless units, then reads as: $\tilde{T}(x, y, z, t) = 1 - z + \theta(x, y, z)$. Figure 1 shows the combined plot of the total temperature field $[\tilde{T}(x, y, z, t)]$ and the velocity field $[\mathbf{v}(x, y, z, t)]$ simultaneously at two different instants for a water based nanofluids ($Pr_{nf} = 6.4$) for $Ra_{nf} = 5 \times 10^5$ and $Q_{nf} = 100$. The dimensions of the simulation box are $L \times L \times 1$, where $L = \frac{2\pi}{k_c(Q_{nf})} = 1.697$ for $Q_{nf} = 100$. The colour bar that is given in each of the viewgraphs shows the temperature field at different points in the convecting fluid. Red, blue, and other colours stand for the hottest, coolest, and intermediate temperatures, respectively. The arrows show the flow directions at the outer surfaces of the simulation box. Thin thermal boundary layers near the lower and upper surfaces of the simulations box are clearly visible. There are generations of thermal plumes (red coloured patches) at the lower boundaries if the temperature gradient is large enough. They are of different sizes and they appear quite irregularly at different locations on the horizontal plate. This also contributes to the fluctuations of fields. There is no viscous boundary layer because of the use of stress-free boundary conditions on the velocity field. Two viewgraphs in Figure 1 confirm the unsteady magnetoconvection. The flow structure is changing with time drastically. Figure 2 shows the variation of flow structures for $Pr_{nf} = 6.4$ and $Ra_{nf} = 5 \times 10^5$ and for two different values of Chandrasekhar number (Q_{nf}). Figure 2a shows the total temperature field $[\tilde{T}(x, y, z)]$ and the velocity field $[\mathbf{v}(x, y, z)]$ in the simulation at a randomly chosen time for $Q_{nf} = 100$. The flow structure that is shown in Figure 2b is for $Q_{nf} = 250$.

Figure 3 shows the temporal variations of three global quantities for $Ra = 5.0 \times 10^5$, $Pr = 4.0$ and for two different values of Q : (1) the kinetic energy per unit mass (E), (2) the convective entropy per unit mass (E_Θ), and (3) the Nusselt number (Nu). All fields are recorded on all grid points and then the global quantities are computed by averaging over the three-dimensional simulation box. The first two sets of curves (from the top) show the variation of E with dimensionless time for two different values of Q . The red curve is for $Q = 100$ and the blue curve is for $Q = 400$. The energy signal varies irregularly with time. They show appreciable fluctuations. The mean of kinetic energy decreases with increase in Q . The fluctuations of kinetic energy also decreases with an increase in Q . Curves in the third and fourth rows (from the top) show the temporal variation of E_Θ , while curves in the fifth and sixth rows display the temporal signal of Nu . They also vary irregularly with time. The mean values of the convective entropy per unit mass as well as the Nusselt number decrease with an increase in Q . Their fluctuations also decrease, as Q is raised.

Figure 4 displays the power spectrum densities (PSD) for the global (spatially averaged) quantities in the frequency (f) space for several values of Ra , Pr and Q . The PSDs of the fluid speed $[E(f) = |\mathbf{v}(f)|^2]$ are shown in Figure 4a. As the thermal energy is injected slowly in the fluid, the spectra show a small slope at low frequencies. In a small frequency window (approximately, $0.04 \lesssim f \lesssim 1.0$), the slope of curves $E(f) - f$ on the log-log scale varies between -3.2 to -5.1 . The energy spectra $[E(f)]$ have more noise in this frequency range. It may be due to irregularity in the size and frequency of thermal plumes from a particular position on the lower boundary. The spectra for nanofluids ($Pr_{nf} = 4.0$ and 6.4) show more noise. Smaller values of the thermal diffusivity of the fluid lead to an enhancement of the thermal noise, which makes the spectra noisier at lower frequencies. However, the $E(f)$ is found to have insignificant noise for $1 < f < 200$. The frequency spectrum of energy per unit mass $[E(f)]$ decays slowly in this regime. This may be due to the box averaging of the perturbative fields, and it is different than the behaviour near horizontal boundaries. The PSD $[E(f)]$ of the kinetic energy scales with frequency (f) almost as $f^{-\alpha}$ with $\alpha \approx 2$. The scaling behaviour is valid for more than two decades. The PSD shows a clear scaling behaviour for $f > 1$. The scaling exponent is independent of Pr , Ra and Q in this frequency window. Table 1 gives the numerically computed values of the

exponent (α) for different values of Ra, Pr, and Q. A similar scaling law [$E(f) \sim f^{-2}$] was also observed in rotating Rayleigh–Bénard convection [16].

Figure 4b shows the PSDs of the convective entropy [$E_{\Theta}(f) = |\theta(f)|^2$] of the fluid in the frequency space for different values of Ra, Pr and Q. Its power spectra is also noisy in the dimensionless frequency range $0.04 < f < 1.0$. The slope on the log-log scale varies between -5.9 and -6.4 . However, for $f > 1.0$, E_{Θ} scales with frequency as $f^{-\beta}$ with $\beta \approx 2$. Table 1 lists the numerically computed values of the exponent β . Interestingly, the power spectra of the temperature fluctuations are also found to vary as f^{-2} in the rotating RBC experiments [2,16]. The temperature of convecting fluid near the horizontal plates in RBM was measured in experiments on magnetoconvection [17]. The frequency spectra of the temperature field near the horizontal plates vary clearly as f^{-2} for $Q = 0$. Even for very small values of Q ($Q \sim 10^{-3} - 10^{-4}$), this scaling regime shrinks drastically. The data points for the temperature field were measured locally in this experiment. The frequency spectra of local quantities near the boundary are known to decay faster [5]. The convective entropy is a global quantity and it is computed by taking an average over the simulation box. That is why the power law for the temperature field recorded locally in the experiment [17] may reflect the behaviour in a thin boundary layer near the horizontal plates. In addition, we have used stress-free conditions on the velocity field on the horizontal plates. We only have thermal boundary layers. These may be reasons for disagreement in the power behaviour.

Figure 4c shows the power spectral densities of the thermal flux [Nusselt number, $Nu(f)$] for several values of Ra, Pr, and Q. PSDs of the Nusselt number also show the scaling behaviour. The PSDs are noisy, as in the case of energy and entropy signals, for dimensionless frequencies $0.04 < f < 1.0$, if $Pr > 1$. The scaling exponent varies between -4.5 to -6.4 in this frequency window. However, for higher values of dimensionless frequency ($1 < f < 200$), the spectra for thermal flux [$Nu(f)$] also shows very clear scaling: $Nu(f) \sim f^{-\gamma}$, with $\gamma \approx 2$. Table 1 shows the values of the exponent γ that is computed in DNS. The measurements of the spectra of thermal flux in RBC also shows the similar scaling law [5]. The scaling behaviour for all global quantities for Rayleigh–Bénard magnetoconvection shows a similar power law. This is also observed in experiments in different systems [2,5] as well as in numerical simulations [15,16]. The power spectra of systems showing self-organised criticality [28] scale with frequency as f^{-1} , which is different than the scaling behaviour in the hydrodynamic systems discussed here.

The scaling law showing the variation of the power spectra as f^{-2} starts at a critical frequency (f_c) for different values of Q. Figure 5 shows the variation of f_c for $E(f)$, $E_{\Theta}(f)$, and $Nu(f)$ with Q for two different sets of Ra and Pr. The critical frequency $f_c(E)$ decreases, as Q is increased (see Figure 5a). Figure 5b,c show the variations of $f_c(E_{\Theta})$ and $f_c(Nu)$, respectively, with Q. The values of critical frequencies are different for $E(f)$, $E_{\Theta}(f)$ and $Nu(f)$. However they all decrease with an increase in Q for given values of Ra and Pr. A vertical magnetic field is known to delay the onset of fluid flow in RBC [18]. The external magnetic field suppresses the fluid motion, which leads to a decrease in $f_c(Q)$, as Q is raised.

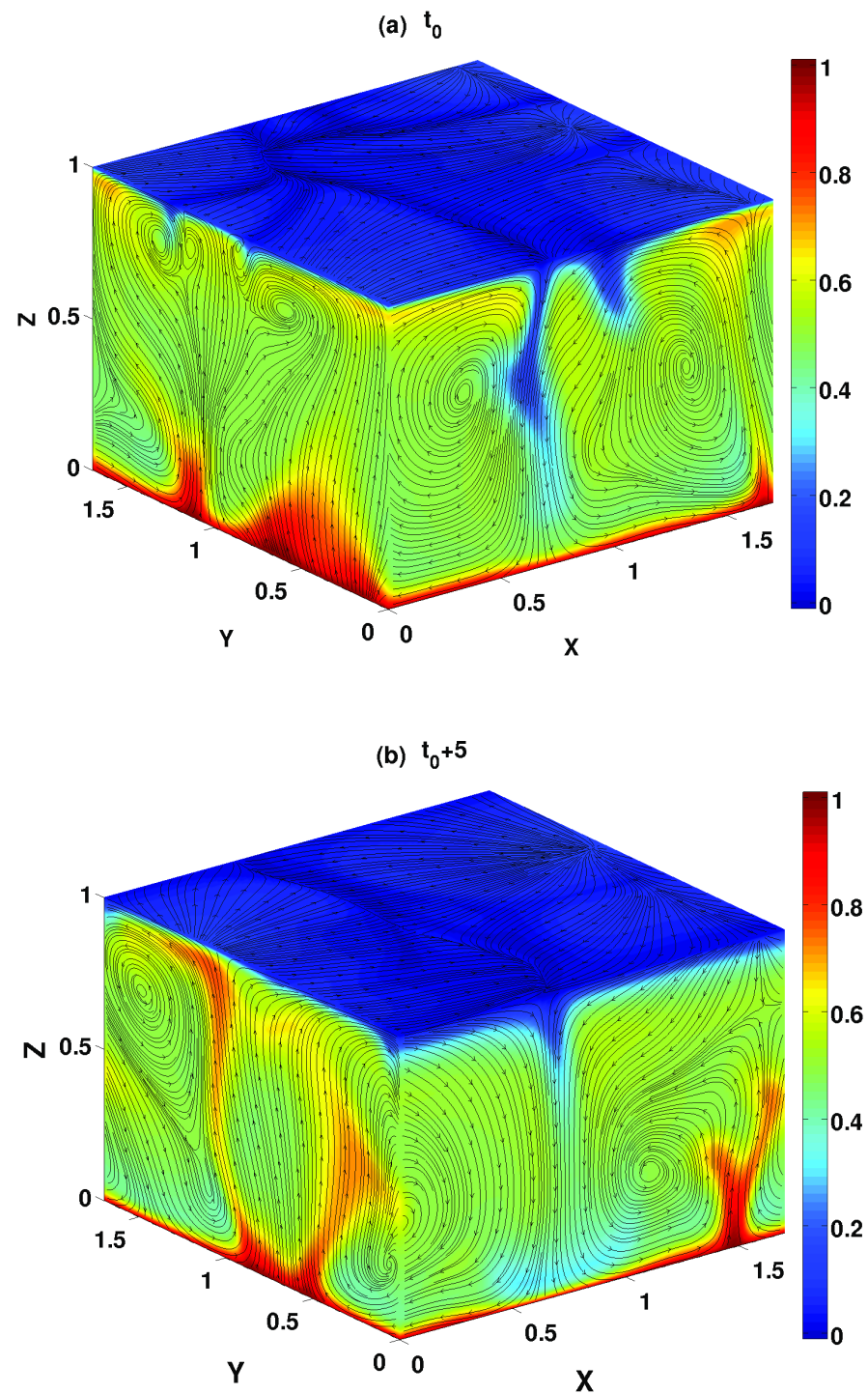


Figure 1. Plot of the total temperature field $[T(x, y, z, t)]$ and velocity field $[v(x, y, z, t)]$ at dimensionless time (a) $t = t_0$ and (b) $t = t_0 + 5$ in the simulation box for a water-based nanofluid $[Ra_{nf} = 5.0 \times 10^5, Pr_{nf} = 6.4$ and $Q_{nf} = 100]$. Colour bars describe the temperature distributions in the convecting fluid. Arrows show the directions of the fluid flow.

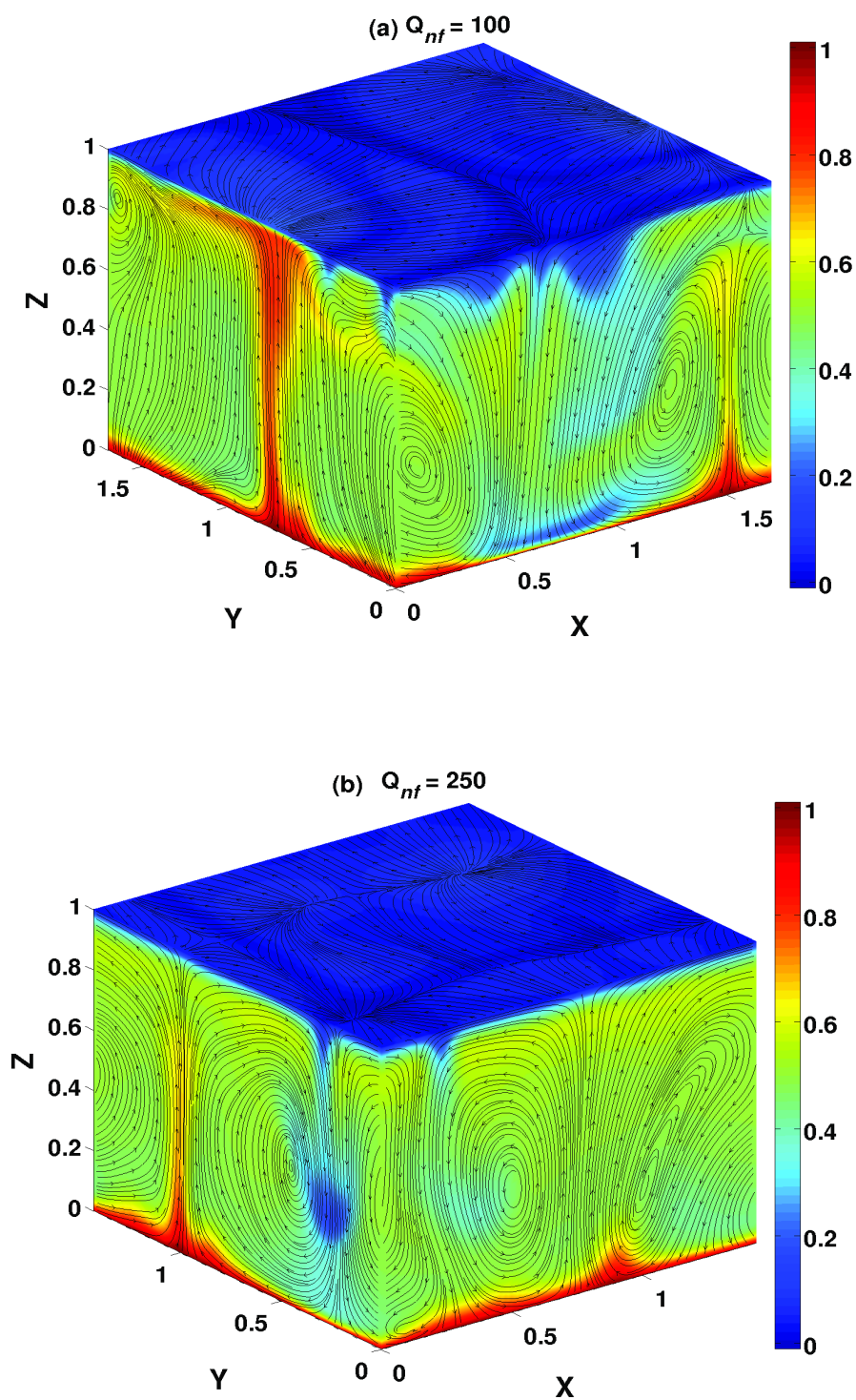


Figure 2. Plot of the total temperature field $[T(x, y, z, t)]$ and velocity field $[v(x, y, z, t)]$ for different values of Chandrasekhar's number: (a) $Q_{nf} = 100$ and (b) $Q_{nf} = 250$ in the simulation box for a water-based nanofluid $[Ra_{nf} = 5.0 \times 10^5$ and $Pr_{nf} = 6.4$. Colour bars and arrows describe the distribution of total temperature field (\bar{T}) and fluid velocity (\mathbf{v}), respectively, at a given time t .

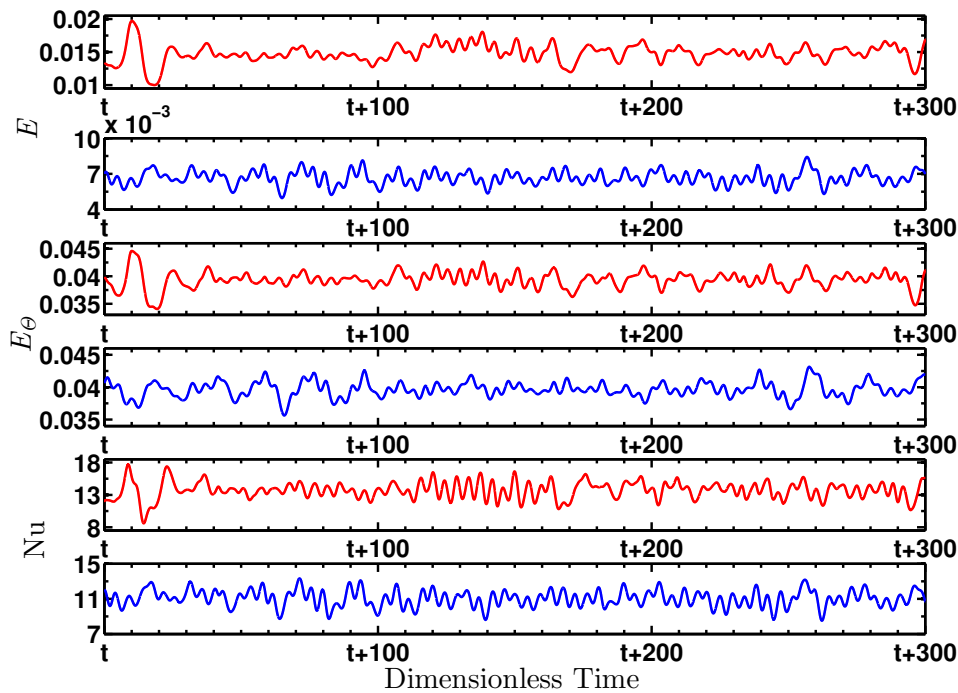


Figure 3. Temporal variations of the kinetic energy (E), entropy (E_{Θ}) and Nusselt number (Nu) in a water-based nanofluid of Prandtl number $Pr_{nf} = 4.0$ for the Rayleigh number $Ra_{nf} = 5.0 \times 10^5$. The red curves are for the Chandrasekhar number $Q_{nf} = 100$, while the blue curves are for $Q_{nf} = 400$.

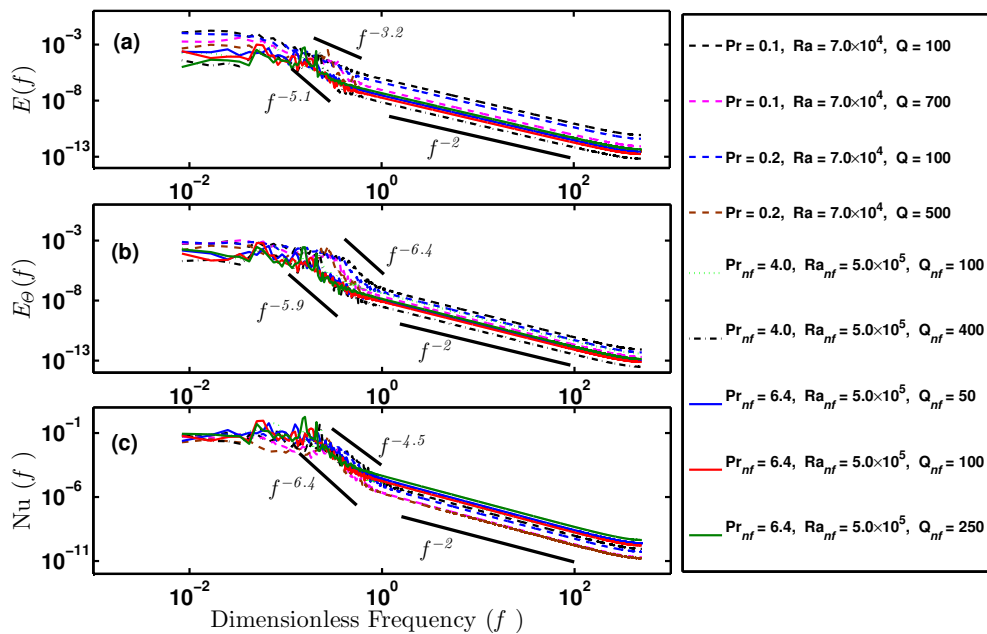


Figure 4. Frequency power spectral densities (PSD) of (a) the energy per unit mass [$E(f) = |v(f)|^2$], (b) the convective entropy per unit mass [$E_{\Theta}(f) = |\theta(f)|^2$], and (c) thermal flux [$Nu(f)$] in the frequency space for Earth’s liquid outer core ($Pr \sim 0.1, 0.2$) and for water-based nanofluids with less than 8% of spherical copper nanoparticles ($Pr_{nf} \sim 4.0, 6.4$) of for different values of Ra , Q , and Pr .

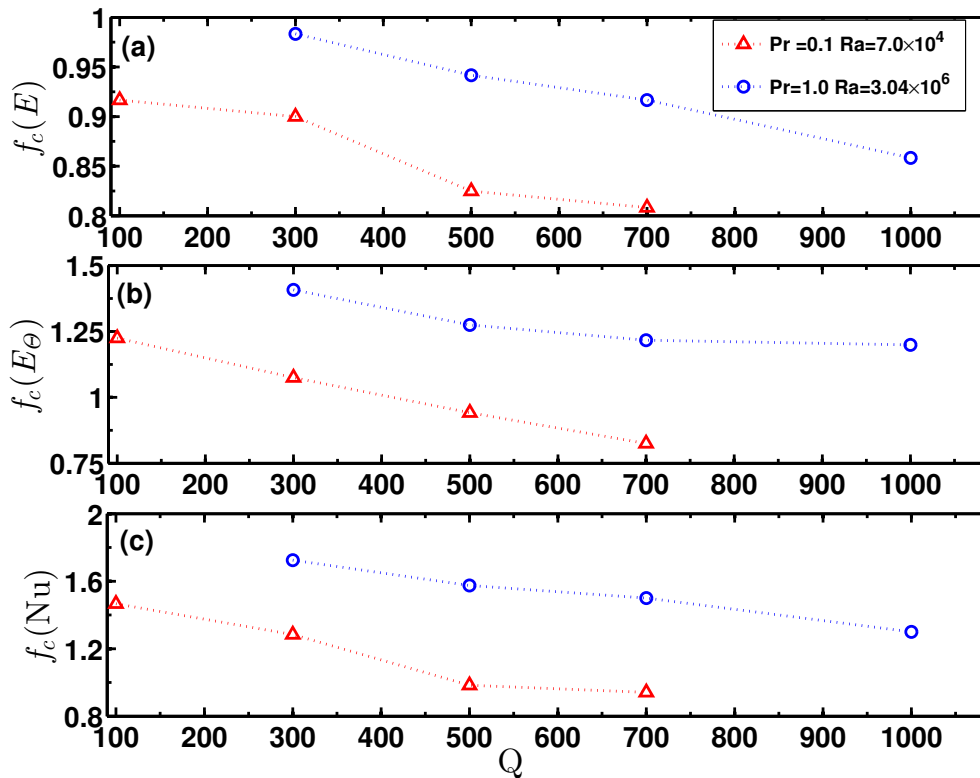


Figure 5. Variation of critical values of the dimensionless frequencies: (a) $f_c(E)$, (b) $f_c(E_\Theta)$, and (c) $f_c(Nu)$ for the frequency spectra of kinetic energy $[E(f)]$, entropy spectra $[E_\Theta(f)]$, and thermal flux $[Nu(f)]$, respectively, with the Chandrasekhar number $[Q]$ for Prandtl number (Pr) = 0.1 [red triangles] and 1.0 [blue circles].

Table 1. List of Prandtl number Pr, Chandrasekhar number Q, Rayleigh number Ra, exponents of Kinetic energy (α), exponents of Entropy (β), and exponents of Nusselt number (γ).

Pr	Ra	Q	Exponent α	Exponent β	Exponent γ
0.1	7.0×10^4	100	1.97	1.97	1.96
		300	1.97	1.97	1.97
		500	1.96	1.96	1.97
		700	1.96	1.97	1.97
0.2	7.0×10^4	100	1.96	1.97	1.96
		300	1.97	1.97	1.96
		500	1.96	1.96	1.96
		700	1.96	1.97	1.96
1.0	3.04×10^6	300	1.96	1.97	1.96
		500	1.96	1.97	1.96
		700	1.97	1.96	1.96
		1000	1.96	1.97	1.97
2.0	3.04×10^6	500	1.96	1.96	1.96
		700	1.96	1.96	1.96
		1000	1.96	1.97	1.96
4.0	5.0×10^5	100	1.96	1.97	1.96
		200	1.96	1.97	1.97
		400	1.96	1.97	1.97
6.4	5.0×10^5	50	1.96	1.97	1.96
		100	1.97	1.97	1.96
		250	1.97	1.96	1.97

5. Conclusions

The results of DNS on Rayleigh–Bénard magnetoconvection show that frequency spectra of global quantities (the kinetic energy $E(f)$, convective entropy $E_{\Theta}(f)$, and the Nusselt number $\text{Nu}(f)$) vary differently in different frequency windows. At low frequencies, the thermal energy enters slowly into the moving fluid. The frequency spectra, therefore have a small slope at low frequencies. In a narrow intermediate frequency range, the spectral densities of global quantities decrease sharply with frequency (f). They show power law behaviour. However, the scaling exponents are dissimilar for different global quantities. The energy spectrum $[E(f)]$ varies with the frequency (f) as $E(f) \sim f^{-\zeta}$, with $3.2 \leq \zeta \leq 5.1$. Scaling behaviour for the convective entropy and Nusselt number are $E_{\Theta}(f) \sim f^{-\eta}$, with $5.9 \leq \eta \leq 6.4$ and $\text{Nu}(f) \sim f^{-\zeta}$ with $4.5 \leq \zeta \leq 6.4$, respectively. For frequencies above a critical frequency f_c , all global quantities show universal scaling behaviour. The critical values $f_c(E)$, $f_c(E_{\Theta})$, and $f_c(\text{Nu})$ are different for kinetic energy, convective entropy, and the Nusselt number, respectively. The spectra of all three global quantities scale with frequency as f^{-2} . The scaling exponent of -2 at higher frequencies are independent of Ra , Pr , and Q . The scaling behaviour of the global quantities at higher frequencies appears to be a universal feature in turbulent flows. The results that are presented here may also be relevant for some problems of geophysics, water-based nanofluids, crystal growth, and magnetohydrodynamics.

Author Contributions: Conceptualization: K.K.; Methodology: S.D. and K.K.; Simulations: S.D.; Analysis: K.K. and S.D.; Writing: K.K. and S.D. All authors have read and agreed to the published version of the manuscript.

Funding: This research received partial funding from IIT Kharagpur, Kharagpur West Bengal, India.

Institutional Review Board Statement: Not applicable.

Informed Consent Statement: Not applicable.

Data Availability Statement: The data that support the findings of this study are available on request from SD.

Conflicts of Interest: The authors declare no conflict of interest.

References

1. Botet, R.; Ploszajczak, M. *Universal Fluctuations (The Phenomenology of Hadronic Matter): World Scientific Lecture Notes in Physics*; World Scientific: Singapore, 2002.
2. Boubnov, B.M.; Golitsyn, G.S. Temperature and velocity field regimes of convective motions in a rotating plane fluid layer. *J. Fluid Mech.* **1990**, *219*, 215–239. [[CrossRef](#)]
3. Fauve, S.; Laroche, C.; Castaing, B. Pressure fluctuations in swirling turbulent flows. *J. Phys. II* **1993**, *3*, 271–278. [[CrossRef](#)]
4. Niemela, J.J.; Skrbek, L.; Sreenivasan, K.R.; Donnelly, R.J. Turbulent convection at very high Rayleigh numbers. *Nature* **2000**, *404*, 837–840. [[CrossRef](#)] [[PubMed](#)]
5. Aumaitre, S.; Fauve, S. Statistical properties of the fluctuations of the heat transfer in turbulent convection. *Europhys. Lett.* **2003**, *62*, 822–828. [[CrossRef](#)]
6. Tanriverdi, V.; Tilgner, A. Global fluctuations in magnetohydrodynamic dynamos. *New J. Phys.* **2011**, *13*, 033019. [[CrossRef](#)]
7. Gerolymos, G.; Vallet, I. Pressure, density, temperature and entropy fluctuations in compressible turbulent plane channel flow. *J. Fluid Mech.* **2014**, *757*, 701–746. [[CrossRef](#)]
8. Kakac, S.; Pramuanjaroenkij, A. Review of convective heat transfer enhancement with nanofluids. *Int. J. Heat Mass Transf.* **2009**, *52*, 3187–3196. [[CrossRef](#)]
9. Tsimring, L.S. Noise in biology. *Rep. Prog. Phys.* **2014**, *77*, 026601. [[CrossRef](#)]
10. Deco, G.; Kringelbach, M.L.; Jirsa, V.K.; Ritter, P. The dynamics of resting fluctuations in the brain: Metastability and its dynamical cortical core. *Sci. Rep.* **2017**, *7*, 3095. [[CrossRef](#)]
11. Damon, P.E.; Lerman, J.C.; Long, A. Temporal fluctuations of atmospheric ^{14}C : Causal factors and implications. *Ann. Rev. Earth Planet Sci.* **1978**, *6*, 457–494. [[CrossRef](#)]
12. Tyler, R.H.; Boyer, T.P.; Minami, T.; Zweng, M.M.; Reagan, J.R. Electrical conductivity of the global ocean. *Earth Planet Space* **2017**, *69*, 156. [[CrossRef](#)]
13. Mobilia, M.; Georgiev, I.T.; Täuber, U.C. Phase Transitions and Spatio-Temporal Fluctuations in Stochastic Lattice Lotka–Volterra Models. *J. Stat. Phys.* **2007**, *128*, 447–483. [[CrossRef](#)]

14. Brennecke, F.; Mottl, R.; Baumann, K.; Landig, R.; Donner, T.; Esslinger, T. Real-time observation of fluctuations at the driven-dissipative Dicke phase transition. *Proc. Natl. Acad. Sci. USA* **2013**, *110*, 11763–11767. [[CrossRef](#)]
15. Das, S.; Kumar, K. Thermal flux in unsteady Rayleigh–Bénard magnetoconvection. *Int. J. Heat Mass Transf.* **2019**, *142*, 118413. [[CrossRef](#)]
16. Pharasi, H.K.; Kumar, K.; Bhattacharjee, J.K. Frequency spectra of turbulent thermal convection with uniform rotation. *Phys. Rev. E* **2014**, *90*, 041004(R). [[CrossRef](#)]
17. Burr, U.; Müller, U. Rayleigh–Bénard convection in liquid metal layers under the influence of a vertical magnetic field. *Phys. Fluids* **2001**, *13*, 3247–3257. [[CrossRef](#)]
18. Chandrasekhar, S. *Hydrodynamic and Hydromagnetic Stability*; Oxford University Press: London, UK, 1961.
19. Fauve, S.; Laroche, C.I.; Libchaber, A.; Perrin, B. Chaotic Phases and Magnetic Order in a Convective Fluid. *Phys. Rev. Lett.* **1984**, *52*, 1774–1777. [[CrossRef](#)]
20. Weiss, N.O.; Proctor, M.R.E. *Magnetoconvection*; Cambridge University Press: Cambridge, UK, 2014.
21. Basak, A.; Raveendran, R.; Kumar, K. Rayleigh–Bénard convection with uniform vertical magnetic field. *Phys. Rev. E* **2014**, *90*, 033002. [[CrossRef](#)]
22. Maxwell, J. *A Treatise on Electricity and Magnetism*; Oxford University Press: London, UK, 1873.
23. Selimefendigil, F.; Öztop, H.F. Numerical study of MHD mixed convection in a nanofluid filled lid driven square enclosure with a rotating cylinder. *Int. J. Heat Mass Transf.* **2014**, *78*, 741–754. [[CrossRef](#)]
24. Brinkman, H. The viscosity of concentrated suspensions and solutions. *J. Chem. Phys.* **1952**, *20*, 571–581. [[CrossRef](#)]
25. Canuto, C. *Spectral Methods in Fluid Dynamics: Springer Series in Computational Physics*; Springer: Berlin/Heidelberg, Germany, 1988.
26. Olson, P.; Glatzmaier, G.A. Magnetoconvection and thermal coupling of the Earth’s core and mantle. *Phil. Trans. R. Soc. Lond. A* **1996**, *354*, 1413–1424.
27. Lan, C.W.; Kou, S. Heat transfer, fluid flow and interface shapes in floating-zone crystal growth. *J. Crystal Growth* **1991**, *108*, 351–366. [[CrossRef](#)]
28. Bak, P.; Tang, C.; Wiesenfeld, K. Self-organized criticality. *Phys. Rev. A* **1988**, *38*, 364–374. [[CrossRef](#)] [[PubMed](#)]